Sensors & Actuators: A. Physical 365 (2024) 114835

Contents lists available at ScienceDirect

Sensors and Actuators: A. Physical

journal homepage: www.journals.elsevier.com/sensors-and-actuators-a-physical

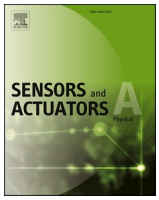

Optimizing contact angle changes for droplet actuation by optoelectrowetting (OEW): A numerical multi-parameter analysis

E. Oliveira *, C. Doering, H. Fouckhardt

Integrated Optoelectronics and Microoptics Research Group, Physics Department, University of Kaiserslautern-Landau (RPTU), P.O. Box 3049, D-67653 Kaiserslautern, Germany

ARTICLE INFO

Keywords:
Microfluidics
Optoelectrowetting (OEW)
Electrowetting on dielectric (EWOD)
Droplet actuation

ABSTRACT

With the transition of fluid-capillary-based "Lab on a chip 1.0" concepts in analytical chemistry to "Lab on a chip 2.0" approaches relying on distinct fluid droplets ("digital microfluidics", DMF), the need for reliable methods for droplet actuation has increasingly come into focus. One possible approach is based on "electrowetting on dielectric" (EWOD). This technique has the disadvantage that any possible desired later positions of the droplets on the chip have to be defined prior to chip realization because one of the EWOD electrode layers has to be structured accordingly. "Optoelectrowetting" (OEW) goes a step further in the sense that the later droplet positions do not have to be known before, and none of the electrode layers has to be structured. Instead, the electrical parameters of the layer sequence can be altered locally by an impinging (and movable) light spot. Although some research groups have succeeded in demonstrating OEW actuation of droplets, the optimization of the relevant parameters of the layer sequence and the droplet – at least half a dozen parameters altogether – is tedious and not straight-forward. In this contribution, for optimization purposes, the equations governing OEW are revisited and altered again, e.g., by numerical implementation of the experimentally well-known saturation of the contact angle change. Additionally, a Nelder-Mead algorithm is applied to find the parameters, on which the optimization has to focus to maximize contact angle changes and, thus, mechanical forces on the droplets. The numerical investigation yields diverse results, e.g., the finding that the droplet's contact area on the dielectric layer has a strong influence on the contact angle change and the question whether the droplet is pulled or pushed. Moreover, the interplay between frequency and amplitude of the applied rectangular alternate voltage is important for optimization.

1. Introduction

The electrowetting effect, which is behind the "optoelectrowetting" (OEW) principle, was first explained by Lippmann in 1875 [1], even though the term "electrowetting" was coined much later by Beni and Hackwood [2]. This laid the foundation for its use in diverse areas such as "digital microfluidic" (DMF) systems [3,4], variable optical liquid lenses [5], beam steering devices [6], among other applications [7–9]. Especially interesting are also [10,11]. In [10] electro-optical devices are tuned over a wide wavelength range by tuning the resonance of silver nanoslits by moving droplets in and out of the optical path with via actuation by EWOD (electrowetting on dielectric – quasi as a predecessor to OEW). In [11] of the same group this principle is used to tune the resonance of a THz metamaterial sample.

The construction of traditional electrowetting on dielectric (EWOD) devices often encounters challenges due to the intricate lithography steps required [3]. A promising solution emerged in the form of lithography-free devices, using light to modify the local electrical conductivity and capacitance with the help of an additional photoconductive layer, typically a-Si:H, to induce contact angle changes [4,12]. This approach is known as optoelectrowetting.

One of the remarkable achievements in this area was the development of a device capable of handling 96 droplets in parallel using an optical projector [13]. Further contributions by the same group showed the so-called "co-planar" optoelectrowetting device, in which a regular metallic grid is introduced between a hydrophobic coating and the dielectric layer to act as a shunt circuit. This application removes the need for a topmost electrode (then usually an indium-tin-oxide (ITO) layer). Droplet manipulation speeds of up to 4.5 cm/s were achieved this way [14,15].

* Corresponding author.
E-mail address: candido@rptu.de (E. Oliveira).

https://doi.org/10.1016/j.sna.2023.114835
Received 1 September 2023; Received in revised form 27 October 2023; Accepted 12 November 2023
Available online 17 November 2023

Despite its potential of applications, OEW, its mathematical modeling, and optimization still present significant challenges, given the multitude of device and droplet parameters involved. The intricate relationship between these variables and the resulting contact angle changes and forces on the droplets requires a thorough examination, as discussed, e.g., in [16].

A problem that has often been encountered experimentally, but still not optimally approached numerically is the observed contact angle saturation [7,17,18]. A mathematical model to incorporate such saturation into the Young-Lippmann equation will be needed, if one aims at optimizing the devices.

This manuscript is intended to delve somewhat deeper into the equations governing OEW, offering modifications. We use the mathematical description given in [16] as a basis. We employ, however, some other alterations related to the description of the saturation contact angle.

Moreover, an optimization route for maximizing contact angle changes and forces on the droplets – considering all relevant parameters of the layer sequence of the devices and of the droplets themselves – is presented, which is grounded in non-derivative computational methods. For that, Nelder-Mead simplex optimization procedures are applied to find the parameter ranges, where contact angle changes are at their maximum. Some obvious, but also some less obvious design rules for optimization can be deduced this way.

Among other findings, it turns out that the droplet area projected onto the dielectric layer (i.e., A, which is equivalent to the area of contact of the droplet on the dielectric layer) is more important than might have been expected so far. This might be a severe limitation to the use of OEW, since lab assistants should not be forced to change parameter settings permanently, which, e.g., might be provoked by even minor droplet evaporations. On the other hand, parameter ranges might be sought after where value tolerances are large.

2. The Young-Lippmann model and contact angle saturation

The EWOD effect is commonly modeled by the Young-Lippmann (YL) equation:

$$\cos\theta_{YL} = \cos\theta_0 + \frac{1}{2\gamma A} C |V_{D+PC}|^2 \tag{1}$$

in which θ_0 is the initial contact angle (without voltage and light intensity), γ the free energy on the liquid-air interface, C the capacitance, A the droplet's contact area on the dielectric layer, equivalent to its projected area (projected onto the dielectric layer), and V_{D+PC} the potential difference across the device's dielectric (D) and photoconductive (PC) layers. It is common to apply rectangular alternating current (AC) voltages in EWOD and OEW. Their semi-amplitude is denoted by V_{AC}. V_{D+PC} is calculated by considering the different device elements' impedances [16].

For the calculations reported in this article, we assume aqueous droplets, ITO contact layers, a-Si:H as the material for the photoconductive layer, Parylene C from SCS, Woking, UK, as the material for the dielectric layer, covered with a 10 nm thick PTFE (polytetrafluoroethylene) AF® 1600 layer from Sigma Aldrich / Merck, Darmstadt, Germany. This accounts for an initial (experimentally observed) contact angle of 120°.

Fig. 1 shows a 3D model of the OEW device. The different layers are labeled. The area defined by the encompassing line around the blue droplet is the projected droplet area A. The super- and substrate glass slides are coated with the mentioned ITO layers acting as electrodes.

As has been pointed out by many authors [7,17–19], the contact angle cannot be completely reduced to 0° by electrowetting, but rather reaches a certain saturation value $\theta_{sat} > 0$. The latter arises no matter how much the applied voltage is increased [15]. The general explanation for this effect is not yet agreed upon - with some of the explanations

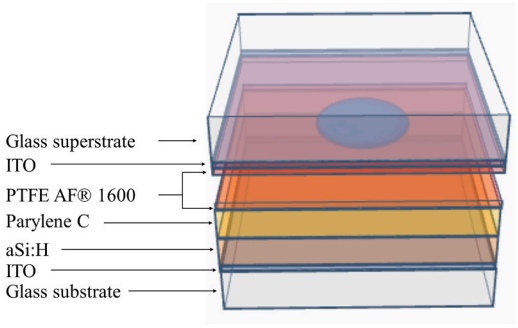

Fig. 1. 3D sketch of the device and its layers.

being a local electrical breakdown of the dielectric layer [20], the elasticity of the substrate [21], or electrochemical processes [17,18,22]. In our contribution, we do not follow our saturation-related approach from [16] and we do not attempt to explain this saturation phenomenon, but rather model it mathematically so that the numerical optimization of the set of parameters is meaningful.

The saturation contact angle is considered to be 60° in this contribution for the mentioned layer sequence, according to experimental observations, e.g., [23,24].

The transition from the YL function (Eq. (1)) to the saturation value is not abrupt, according to experimental observations [17–19]. For the transition, a sigmoid function is applied here, which accounts for a modification of the second summand and an additional third addend on the right side in the YL Eq. (1). However, one more term needs to be considered, since the mere use of the sigmoid function might (depending on the slope of the sigmoid function) result in an unrealistic intermediate dip (see Fig. 2) of the contact angle for increasing voltage. This fourth summand is the first derivative of the same sigmoid function, i.e., a Gaussian function. It is added with a multiplication factor and an exponent, in the examples to be shown in this contribution, both with a

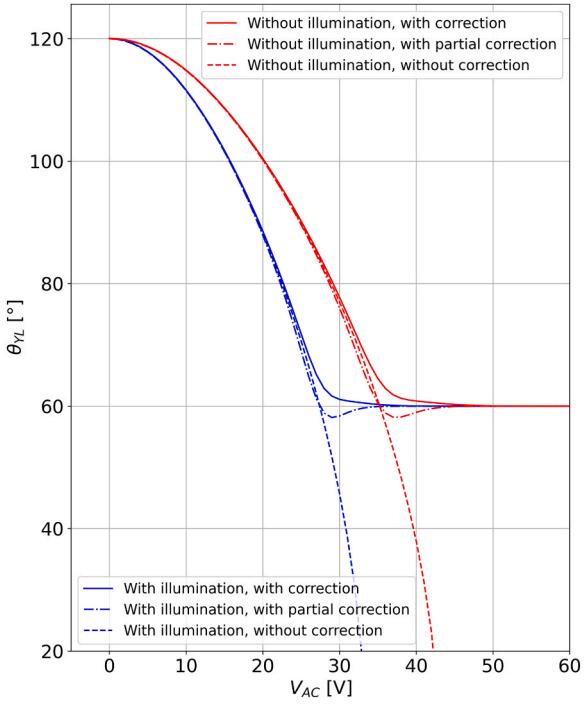

Fig. 2. Contact angle θ_{YL} vs. voltage V_{AC} for cases with (blue) and without illumination (red) with correction for saturation (solid lines), with partial correction (dashed-dotted lines) and without any correction (dashed lines). The used parameter values are given in Table 1.

value of 0.5 to have the smoothest transition to the saturation angle and no dip.

A python program is used to calculate the cosine of the contact angle ($\cos\,\theta_{YL}$) according to the given parameters: AC frequency ν, voltage V_{AC}, thickness d_D of the dielectric layer, thickness d_{PC} and ohmic resistance R_{PC} of the photoconductive layer, which is kept at a constant value of 12 MΩ (inferred from fitting to own experimental data) throughout this article. This value corresponds to the resistance without any illumination; the illuminated ohmic resistance is considered to be a factor of 100 smaller [25]. The overall ohmic resistance is denoted by R_{Path} (which includes the electrical resistances of the ITO contact layers, of the droplet, of the dielectric as well as of the photoconductive layer).

In some more detail:

The sigmoid function $S(\theta_{YL})$ used for corrections is written as:

$$S(\theta_{YL}) = \frac{1}{1 + e^{\frac{\cos\,\theta_{sat} - \cos\,\theta_{YL}}{T}}}, \tag{2}$$

in which T is a scaling factor, in our examples, set to 0.1.

This function returns values close to 0 for small changes in the contact angle with respect to the initial values and close to 1, whenever the unmodified contact angle approaches values significantly smaller than the saturation angle. Note that the value of 0.5 is achieved when $\theta_{YL} = \theta_{sat}$.

The intermediately new expression can be written as:

$$\begin{aligned} \cos\,\theta_{YL} =\ & \cos\,\theta_0 \\ +(1 - S(\theta_{YL}))\cdot & \left(\frac{1}{2\gamma A} C|V_{D+PC}|^2\right), \\ +S(\theta_{YL})\cdot & (\cos\,\theta_{sat} - \cos\,\theta_0) \end{aligned} \tag{3}$$

As mentioned already above, the rapid decline in contact angle predicted by the YL model is not matched by the alterations from this implementation. To address this issue, we have added even a fourth term, i.e., the first derivative of the sigmoid function, which results in a Gaussian function $S'(\theta_{YL})$:

$$S'(\theta_{YL}) = S(\theta_{YL})\cdot(1 - S(\theta_{YL})) \tag{4}$$

Beyond that, we apply a normalization factor based on the difference between the initial and the saturation contact angle. Thus, the final new expression becomes:

$$\begin{aligned} \cos\,\theta_{YL} =\ & \cos\,\theta_0 \\ +(1 - S(\theta_{YL}))\cdot & \left(\frac{1}{2\gamma A} C|V_{D+PC}|^2\right) \\ +S(\theta_{YL})\cdot & (\cos\,\theta_{sat} - \cos\,\theta_0) \\ +(0.5\cdot S')^{0.5}\cdot & (-\cos\,\theta_{sat})\cdot\frac{\theta_0 - \theta_{sat}}{\theta_0} \end{aligned} \tag{5}$$

This equation – reflecting the influence of pure EWOD – is used both for the cases without and with illumination. In those cases, the relevant angle is called $\theta_{YL\text{-without}}$ or $\theta_{YL\text{-with}}$, respectively.

To show an example of the corrections, Fig. 2 illustrates the calculations without the saturation correction (YL model, presented in Eq. (1)), with partial correction (Eq. (3)), and with all mentioned corrections (Eq. (5)), both for the case with and the case without illumination. The parameters used for those calculations are shown in Table 1, found by the optimization which will be described in Section 3.

Table 1
Optimized values according to the Nelder-Mead algorithm.

Parameter	Optimized value	Unit
ν	243	Hz
V_{AC}	27.39	V
d_D	357	Nm
d_{PC}	2656	Nm
A	1.38 $\cdot 10^{-6}$	m^2

For lower voltages, Eq. (5) aligns well with the YL model predictions (considering an initial angle of 120°). For higher voltages, the stabilization is observed at 60° as desired.

In the laboratories – beyond the contact angle saturation – another phenomenon has been encountered, i.e., a threshold voltage, which has to be applied, before the contact angle starts to change at all [26,27]. This is usually attributed to some kind of friction of the contact line movement [28]. We do not explicitly incorporate this effect in our modified Eq. (5), because we consider it to be well enough taken into account by the zero slope for $V_{AC} = 0$ and the subsequent gradual contact angle decrease of the curves for $V_{AC} > 0$ as shown in Fig. 2.

Moreover, as Krogmann et al. have pointed out in their groundbreaking work [25], – depending on exact parameters – with OEW both pulling (as for pure EWOD) as well as pushing of the droplets is possible.

In our contribution – just for ease of explanations –, we identify a negative contact angle change with pulling, while a positive change is correlated with pushing. This is not exactly true, because the contact line friction alters the situation. But this approximate notation is good enough for finding general rules for OEW use.

3. Numerical optimization: Nelder-Mead simplex algorithm

The OEW-lab-chip situation encounters many parameters. Some of them have already been mentioned above. But there are even more relevant parameters, like the size and the electrical conductivity of the aqueous droplet or the wavelength (thus absorbance in a-Si:H) and intensity of the OEW light beam, as well as the illuminated fraction of the droplet's contact line. Not all parameters are variable in our numerical investigation. E.g., the properties of the materials Parylene C and a-Si:H for the dielectric and the photoconductive layer, respectively, (i.e., their dielectric numbers ε_r) are kept constant throughout, because they are considered optimal by us due to our earlier work [16,29]. With this in mind, we are dealing with a set of six optimizable parameters here:

- AC frequency ν,
- half voltage amplitude V_{AC},
- projected droplet area A,
- thickness d_{PC} of photoconductive layer,
- thickness d_D of dielectric layer and,
- overall ohmic resistance R_{path}.

Due to the high dimensionality of the problem, we employed various computational optimization methods to identify the broadest possible parameter ranges. This was done to locate where contact angle changes are significant and determine the best set of parameters to use. The finally selected method is the so-called Nelder-Mead simplex downhill optimization algorithm [30].

Before going into more detail, it should be stressed here, that our figure of merit is the contact angle change $\Delta\theta$ between the cases with and without illumination – for ease of explanations. That means, we do not explicitly deal with the forces on the droplets, although both quantities are related and the forces should increase the larger the contact angle change is. The expression for $\Delta\theta$ is:

$$\Delta\theta = \theta_{YL,with} - \theta_{YL,without} \tag{5}$$

assuming a specific EWOD voltage. That means that $\Delta\theta$ is a function of voltage V_{AC}.

We also consider a fixed factor f_{area}, which accounts for the illuminated portion of the projected droplet. Fig. 3 shows the dependence of $\Delta\theta$ on f_{area}. Such factor is set to 0.1 for the entirety of this manuscript, since the $\Delta\theta$ values are not significantly different starting from this f_{area} value. We also selected this parameter according to an estimation from our earlier lab work, where 0.1 is typically the minimum illumination factor for droplet actuation [16].

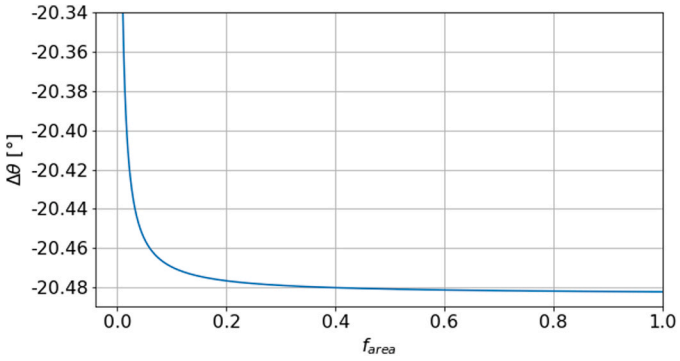

Fig. 3. Contact angle difference ($\Delta\theta$) vs. f_{area}. Abscissa values below 0.1 correspond to high changes in the ordinate, while the contact angle change stabilizes for values > 0.1.

The Nelder-Mead algorithm works as a set of instructions based on the value of the function for a given simplex S [30,31]. A simplex can be defined as a set of parameters that produces outputs for an arbitrary multidimensional function. In our context, we are optimizing the difference $\Delta\theta$ between two outputs from Eq. (5), which represent the cases with and without illumination, respectively, as already mentioned above.

A simplex-based search method will begin with a set of nondegenerate $n+1$ points: $x_0, x_1, \ldots, x_n \in \mathbb{R}_n$ considered as the vertices of a simplex S (each point corresponds to a set of parameters able to produce one output), with the corresponding set of function values at the vertices $f_j = f(x_j)$, for $j = 0,\ldots,n$. The method carries a number of transformations on the working simplex S [30–32] with the intention of decreasing the function values at its vertices. The process is terminated, when the simplex becomes sufficiently small or when the function values become close enough to each other [30].

The algorithm has been implemented by using the scipy python library [33]. The termination condition for the algorithm is set to be the minimum size of the simplex and is set to the default value of 0.0001. The step size for the calculations is directly tied to the initial guess provided to the algorithm, which directly influences the initial simplex and thus, the later calculation steps. Another relevant parameter is the maximum number of iterations, which is set to 10^9. None of the optimization examples that will be shown in this manuscript has exceeded this number of iterations.

To better understand the relation of the contact angle change with respect to specific variables/parameters, we have conducted several numerical optimization procedures using the previously described Nelder-Mead algorithm.

It is important to stress that the term V_{AC} corresponds to the voltage semi-amplitude of a rectangular voltage pulse between $+V_{AC}$ and $-V_{AC}$.

4. A holistic approach

We began our investigation by conducting an optimization process using the Nelder-Mead algorithm with five open parameters, which resulted in the values on Table 1. After identifying this set of optimal parameters, we proceeded to examine the interplay between each pair of these five and their impact on the contact angle change. This approach resulted in a total of 10 distinct plots. For all of those figures, the color-code (third axis) represents the $\Delta\theta$ values.

Whenever d_D, d_{PC}, or A are displayed as axes in the plots below, a logarithmic scale is used and the values shown are "centered" around the optimal values according to Table 1.

Fig. 4 shows how $\Delta\theta$ changes with frequency ν and area A. An interpretation of this chart is that there is a strong dependence of the contact angle difference on the droplet's projected area and thus, of the applied force to the droplet.

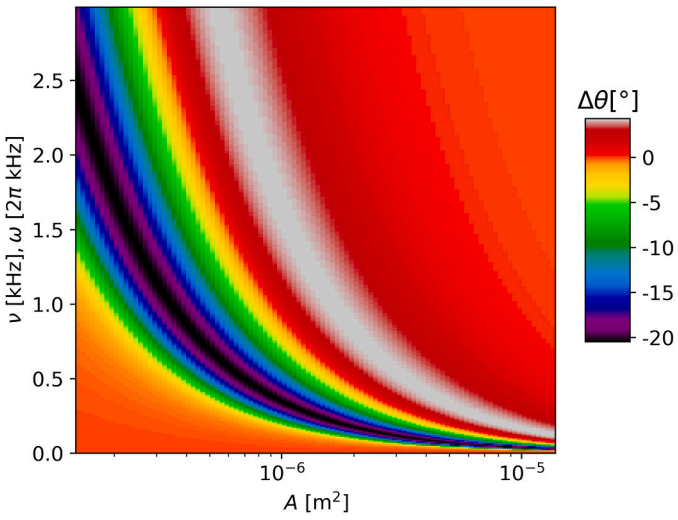

Fig. 4. Dependence of contact angle difference $\Delta\theta$ on frequency ν and projected droplet area A (logarithmic scale). The remaining three parameters are fixed according to Table 1.

Both (strong) pulling and (weak) pushing are to be seen. For smaller droplets, the contact angle change appears to be less influenced by the frequency. In contrast, for larger droplets, only small frequencies and within a narrow frequency range lead to notable changes in the contact angle.

The dielectric layer thickness is the parameter being changed on the abscissa of Fig. 5. Both pushing and pulling are observed depending on the dielectric layer thickness. It is noteworthy that there is a frequency band, ranging from 100 to 500 Hz, where the contact angle difference undergoes significant alterations with dielectric layer thickness. Two bands of dielectric layer thicknesses can be observed: one for pushing (positive values of contact angle difference) and one for pulling (negative values), with similar maximum absolute values.

For Fig. 6, the ordinate is kept as the frequency ν again, while the abscissa consists of the thickness d_{PC} of the photoconductive layer. Pulling has a significantly higher maximum absolute value, but has a more restricted regime of allowed frequencies ν.

Fig. 7 shows the contact angle difference dependency on frequency ν and voltage V_{AC}. Both pushing (with positive $\Delta\theta$ values) and pulling

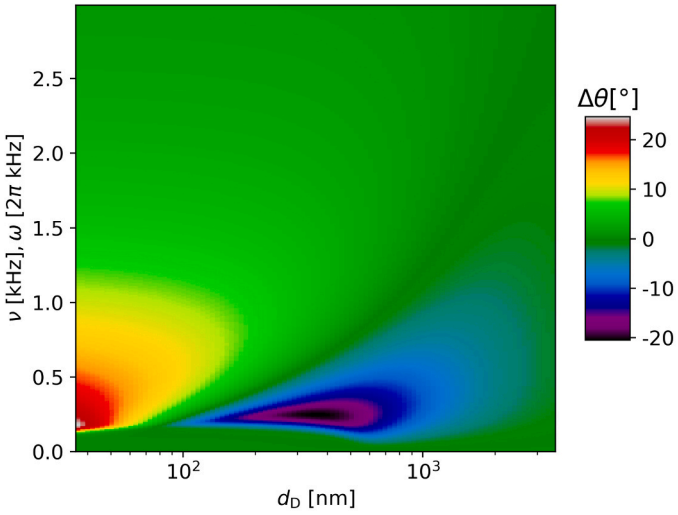

Fig. 5. Dependence of contact angle difference $\Delta\theta$ on frequency ν and thickness d_D of dielectric layer (logarithmic scale). The remaining three parameters are fixed according to Table 1.

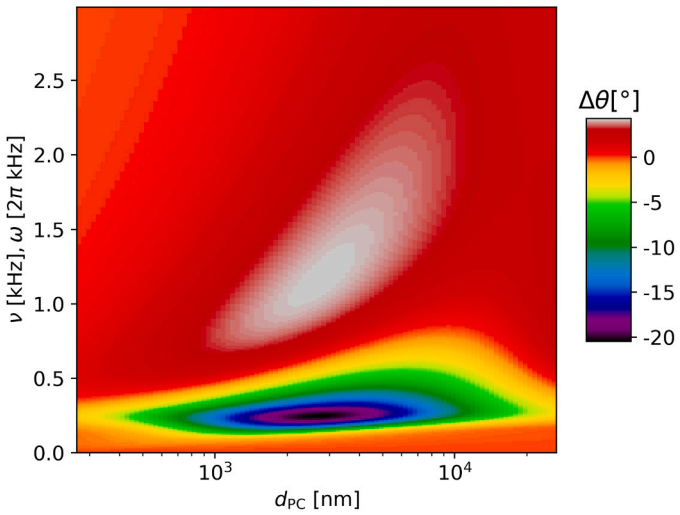

Fig. 6. Dependence of contact angle difference $\Delta\theta$ on frequency ν and thickness d_{PC} of photoconductive layer (logarithmic scale). The remaining three parameters are fixed according to Table 1.

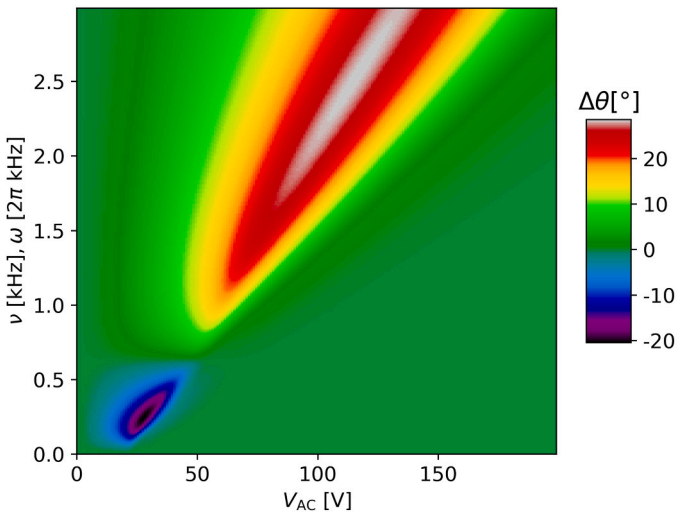

Fig. 7. Dependence of contact angle difference $\Delta\theta$ on frequency ν and voltage V_{AC}, illustrated as a color-plot again. The remaining three parameters are fixed according to Table 1.

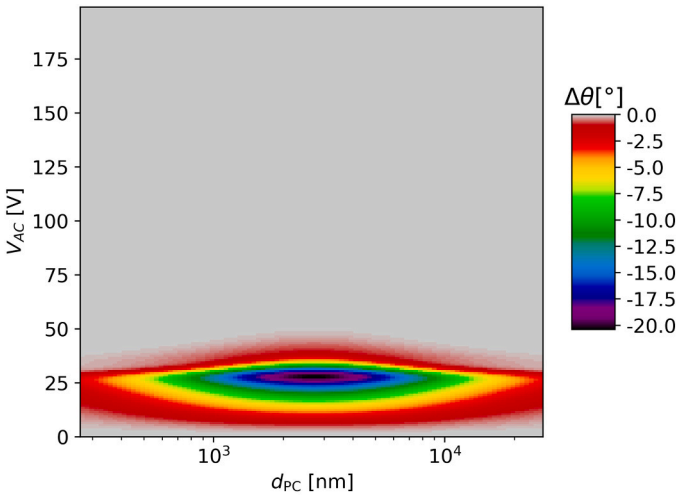

Fig. 8. Color-plot of dependence of contact angle difference $\Delta\theta$ on voltage V_{AC}, and thickness d_{PC} of photoconductive layer. No pushing occurs. The remaining three parameters are fixed according to Table 1.

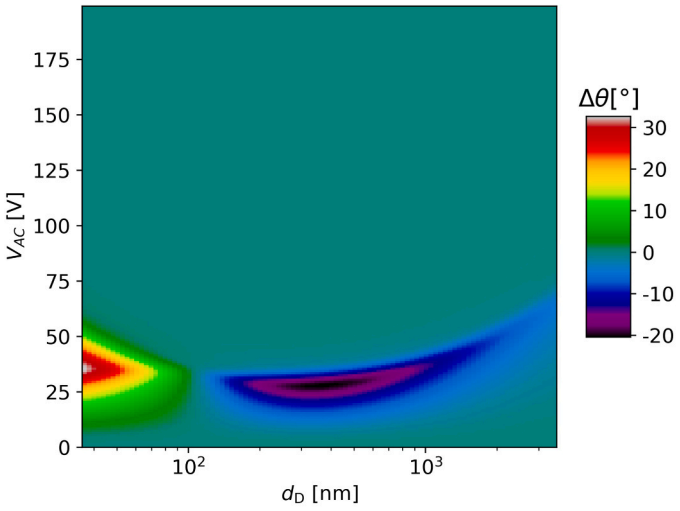

Fig. 9. Color-plot of dependence of contact angle difference $\Delta\theta$ on voltage V_{AC}, and thickness d_D of dielectric layer. The remaining three parameters are fixed according to Table 1.

(with negative $\Delta\theta$ values) are observed. Notably, the region indicating pushing is more extensive than that for pulling and its maximum absolute value is larger, based on this set of parameters.

In contrast to the other graphs in this section, Fig. 8 shows how $\Delta\theta$ is changed with respect to V_{AC} and d_{PC}, and only pulling takes place for this set of parameters. Such finding can come as a surprise, but it just highlights that the dependencies of the contact angle change is not straightforward with any of the given parameters. I.e., $\nu = 243$ Hz here (Table 1), and therefore there is no pushing (see Fig. 7 for comparison).

Furthermore, we see the changes in $\Delta\theta$ with respect to V_{AC} and d_D in Fig. 9. Pushing is observed for small thicknesses of the dielectric layer (below 100 nm) and pulling for intermediate values (from 100 to 1000 nm).

Fig. 10, on its turn, indicates that the optimal range for pulling can be quite extensive with respect to both thicknesses d_{PC} and d_D. There are regions for d_{PC}, where both pushing and pulling can occur. On the other hand, for most specific d_D values, there is either pushing or pulling, not both.

Fig. 11 shows the $\Delta\theta$ dependence with respect to voltage V_{AC} and projected droplet area A. One can see that both pushing and pulling occurs. For larger droplets, a tendency for pushing (at higher voltages) exists, while for smaller areas, pulling (at smaller voltages) is to be observed. This highlights once more that the projected droplet area is fundamental for the operation of the device either on pushing or pulling.

Fig. 12 reveals the $\Delta\theta$ variations with respect to photoelectric layer thickness d_{PC} and projected droplet area A. The chart surface seems to be dominated mostly by pulling, with slight pushing happening for larger droplets and moderate photoconductive layer thicknesses.

Fig. 13 gives an overview of $\Delta\theta$ with respect to dielectric layer thickness d_D and projected droplet area A. For a specific droplet area, both pushing and pulling can occur – with similar strength.

Our findings reveal that the projected area of the droplet exerts a more significant influence on $\Delta\theta$ than initially anticipated. Additionally, the majority of the plots indicate the presence of both pulling and pushing effects. On the other hand, as indicated by Figs. 5, 9, and 10, for a specific thickness d_D of the dielectric layer, there is (more or less) either pulling or pushing.

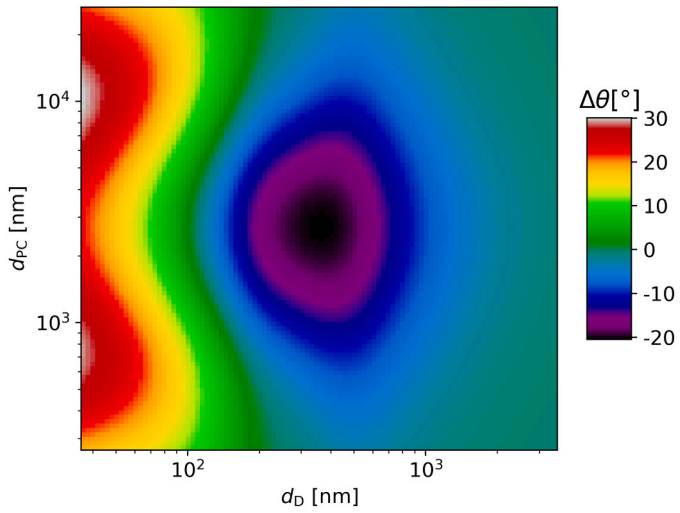

Fig. 10. Color-plot of dependence of contact angle difference $\Delta\theta$ on thickness d_{PC} of photoconductive layer and thickness d_D of dielectric layer. The remaining three parameters are fixed according to Table 1.

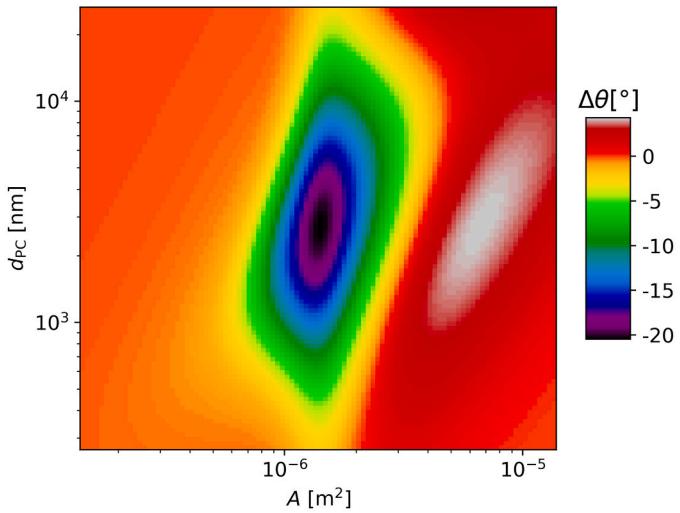

Fig. 12. Color-plot of dependence of contact angle difference $\Delta\theta$ on thickness d_{PC} of photoconductive layer and projected droplet area A. The remaining three parameters are fixed according to Table 1.

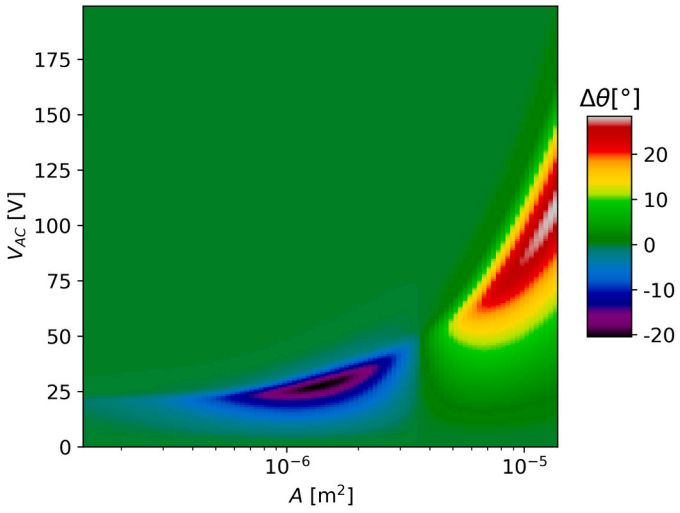

Fig. 11. Color-plot of dependence of contact angle difference $\Delta\theta$ on voltage V_{AC} and projected droplet area A. The remaining three parameters are fixed according to Table 1.

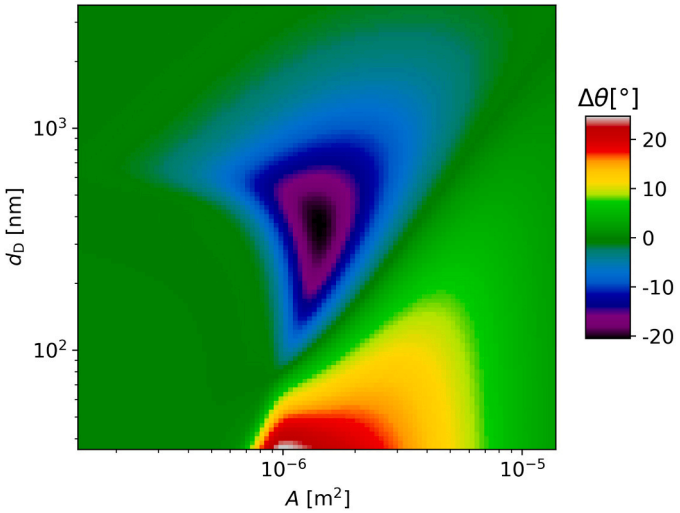

Fig. 13. Color-plot of dependence of contact angle difference $\Delta\theta$ on thickness d_D of dielectric layer and projected droplet area A. The remaining three parameters are fixed according to Table 1.

5. A closer look into some parameters

Finally, we come to a setting, where only voltage V_{AC}, frequency ν, and projected droplet area A are left as the optimizable parameters or variables for three different pre-selected photoconductive layer thicknesses d_{PC}: 4.522 μm, 2.656 μm, and 0.790 μm. The remaining parameters are kept constant as $d_D = 0.357$ μm and $R_{Path} = 5$ MΩ. The reason we focused on these three parameters is that they are the variables that can be directly manipulated in an already-constructed OEW device. This makes them particularly relevant for real-world applications and adjustments post-manufacture.

Fig. 14 illustrates the results for such calculations. Each row stands for a specific thickness of the photoconductive layer. I.e., the photoconductive layer thickness d_{PC} decreases from top to bottom according to the values mentioned above. Each column shows the dependence of the contact angle difference $\Delta\theta$ between the cases with and without illumination at the optimum value given by the Nelder-Mead algorithm. From left to right, the shown dependencies are on frequencyν and voltage V_{AC} (analogous to Fig. 7), frequency ν and projected droplet area A (analogous to Fig. 4), and voltage V_{AC} and projected droplet area A (analogous to Fig. 11), respectively.

From a practical point of view the parameter regions, where the contact angle change is strong, should be as large as possible. Otherwise, droplet actuation might disappear with a small parameter change (e.g., some small amount of droplet evaporation), which would render OEW actuation of droplets non-practical.

The left column in Fig. 14 (a, d, and g) indicates that the useful parameter range is larger the thicker the photoconductive layer is, which might be considered as an important design rule. Furthermore, the parameter regions for pulling (with negative contact angle change) is smaller than that for pushing (positive change).

The middle and the right column in Fig. 14 (b, e, h, and c, f, i) clearly reveal that the droplet area A is a crucial parameter to be adjusted. The middle column even shows that the regions with strong contact angle change are very narrow. I.e., for a specific not too small droplet area the tolerance for the frequency is less than a couple of hundred Hertz. Only for very small droplets the frequency tolerance is larger. Thus, OEW actuation of droplets might be more practical for small droplets below an

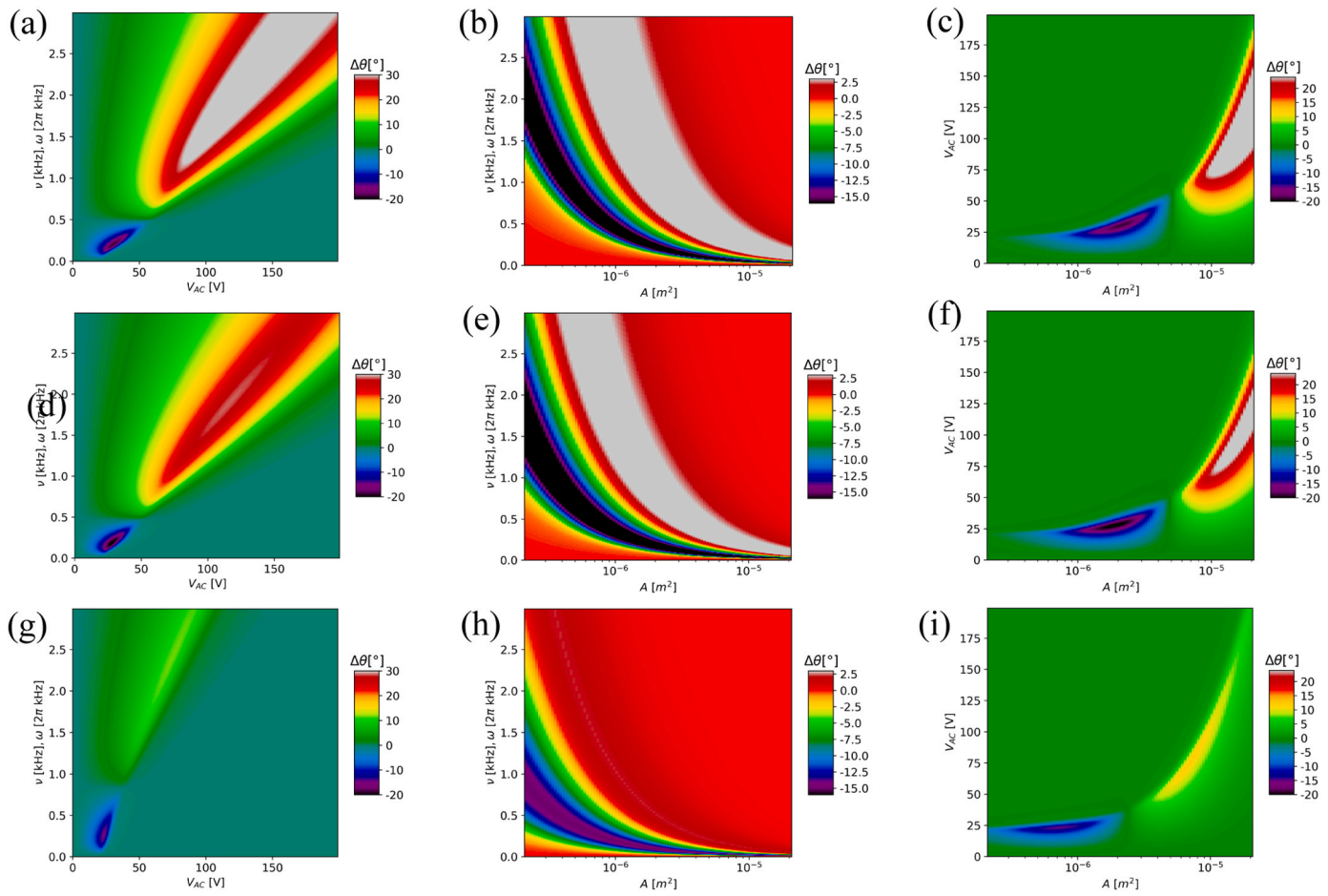

Fig. 14. Color-plots for $\Delta\theta$ dependencies. Photoconductive layer thicknesses d_{PC} values are constant for any row and different from row to row, from top to bottom: 4.522 μm (a, b, and c), 2.656 μm (d, e, and f), and 0.790 μm (g, h, and i). The dependencies are: on frequency and voltage (first column, the values for A are, from top to bottom: 7.24 $\cdot 10^{-7}$ m^2 (a), $1.86 \cdot 10^{-6}$ m^2 (d), and $2.09 \cdot 10^{-6}$ m^2 (g)), on frequency and droplet area (second column, the values for the voltage are, from top to bottom: 22.9 V (b), 27.4 V (e), and 30.2 V (h)) and on voltage and projected droplet area (third column, the values for the frequency are, from top to bottom: 254.5 Hz (c), 181.4 Hz (f), and 202.8 Hz (g)).

area of approximately 4 $\cdot 10^{-6}$ m^2 (corresponding to a radius of roughly 1.1 mm and considering our typical set of parameters). Again, the situation gets better from a practical point of view, the thicker the photoconductive layer is (see design rule above).

The same argument applies in relation to the right-most column in Fig. 14 (c, f, and i). The useful parameter ranges are larger for larger thicknesses of the photoconductive layer. And pushing regimes are more extended than pulling regimes.

Additionally, a periodic wobbling motion of the droplet has been experimentally observed by us under certain sets of parameters. This phenomenon might be related to a slow evaporation of the droplet (in combination with the contact line friction). When the droplet area is reduced due to evaporation, approaching the region, where the maximum effect is anticipated, the electrowetting effect works to decrease the contact angle. This, in turn, expands the droplet's base area. However, this expansion subsequently diminishes the effect, leading to an unstable motion in the droplet.

Fig. 15 illustrates how the projected droplet area A impacts the contact angle difference $\Delta\theta$, using a constant set of parameters (d_D, d_{PC} and R_{path}, set to 0.357 μm, 2.656 μm, and 5 MΩ, respectively) to highlight the maximum positive (for pushing) and maximum negative contact angle changes (for pulling) - represented as orange and blue lines, respectively.

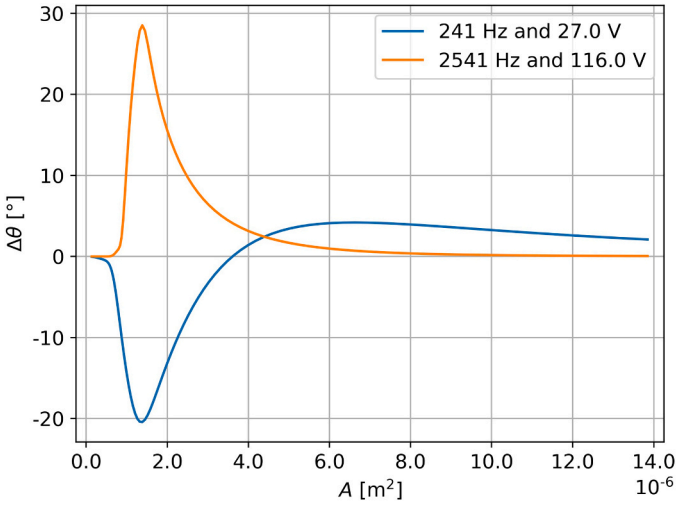

Fig. 15. Contact angle difference $\Delta\theta$ between the case with and without illumination vs. projected droplet area A. The blue line indicates the results for pulling, and the orange one for pushing, respectively.

6. Conclusions

Progress in electrowetting on dielectric (EWOD) and optoelectrowetting (OEW) holds the potential to bring about substantial improvements in fields where liquid droplet manipulation is crucial, such as in diagnostic medicine and modern lab-on-a-chip 2.0 technologies (digital microfluidics, DMF). In our study, we have introduced modifications to the Young-Lippmann model to account for the saturation angle phenomenologically, commonly observed in experiments. This adjustment allows for a better description of realistic situations.

Due to the large number of relevant variable parameters – six in our case – Nelder-Mead simplex optimization algorithms are applied, allowing for pinpointing design rules for OEW chips and experimental procedures.

We have illustrated some of our computational findings, highlighting the relationship between the contact angle change and various parameters.

Some found design and set-up rules are listed as follows:

1 – Droplet's contact area on dielectric layer (called projected droplet area in this contribution) - This emerges as a crucial parameter for optimization. *Smaller* droplet areas (and droplets) allow for a broader frequency range to induce significant contact angle changes, as it can be seen in Fig. 4, for example.

2 – An opposite effect is seen with respect to voltage: If a broad voltage regime is desired, the droplet area should be relatively *large*, as it can be seen in Fig. 7.

3 – Pushing and pulling - Both effects are influenced by the droplet's projected area. However, regions showcasing pushing are consistently more expansive than those indicating pulling. In other words, for a device aimed at pulling, there is a stricter set of conditions that need to be fulfilled.

4 – The thickness of the dielectric layer has a strong influence on the question whether pulling or pushing occurs. It more or less decides which actuation type arises. If both options are desired for the same setting, the user has to accept less optimized contact angle changes (see Fig. 12).

5 – If possible, thicker photoconductive layers are more useful: The allowed parameter ranges become broader for higher d_{PC} values (as shown in Fig. 14).

Additionally, our analysis suggests that the experimentally observed wobbling motion of the droplet might be attributed to an oscillation of the projected droplet area between optimal and suboptimal values, driven by the electrowetting effect itself.

Funding

This research has been funded by the German Research Foundation (Deutsche Forschungsgemeinschaft, DFG) under contract FO 157/65.

CRediT authorship contribution statement

E. Oliveira: Investigation, Methodology, Software, Writing – review & editing. **C. Doering**: Methodology, Visualization, Discussion. **H. Fouckhardt**: Supervision, Writing – review & editing.

Declaration of Competing Interest

The authors declare the following financial interests/personal relationships which may be considered as potential competing interests: Prof. Dr. Henning Fouckhardt, responsible for all authors reports financial support, article publishing charges, equipment, drugs, or supplies, and travel were provided by German Research Foundation.

Data availability

Data will be made available on request.

Acknowledgments

The authors express gratitude for the funding mentioned above. They also thank previous group members who contributed to the OEW topic in its early stage, including Johannes Strassner, Patrick Kuenzig, Lisa Imke Hofmann, and Carina Heisel. Technological assistance of the Nano Structuring Center (NSC) of the University of Kaiserslautern-Landau (RPTU), Germany is acknowledged. Special thanks go to Egbert Oesterschulze and his team at RPTU for allowing us to use their CVD and PECVD machines for preparing dielectric and photoconductive layers for our past experimental devices.

References

[1] G. Lippmann, Relations entre les phénomènes électriques et capillaries, Ann. Chim. Phys. (5) (1875) 494–549.
[2] G. Beni, S. Hackwood, Electro-wetting displays, Appl. Phys. Lett. vol. 38 (4) (1981) 207–209, https://doi.org/10.1063/1.92322.
[3] H.H. Shen, S.K. Fan, C.J. Kim, D.J. Yao, EWOD microfluidic systems for biomedical applications, Microfluid. Nanofluidics vol. 16 (5) (2014) 965–987, https://doi.org/10.1007/s10404-014-1386-y.
[4] S.K. Thio, S.Y. Park, A review of optoelectrowetting (OEW): from fundamentals to lab-on-a-smartphone (LOS) applications to environmental sensors, Lab Chip vol. 22 (21) (2022) 3987–4006, https://doi.org/10.1039/d2lc00372d.
[5] B. Berge, J. Peseux, Variable focal lens controlled by an external voltage: an application of electrowetting, Eur. Phys. J. E vol. 3 (2) (2000) 159–163, https://doi.org/10.1007/s101890070029.
[6] N.R. Smith, D.C. Abeysinghe, J.W. Haus, J. Heikenfeld, Agile wide-angle beam steering with electrowetting microprisms, Opt. Express vol. 14 (14) (2006) 6557, https://doi.org/10.1364/oe.14.006557.
[7] F. Mugele, Fundamental challenges in electrowetting: from equilibrium shapes to contact angle saturation and drop dynamics, Soft Matter vol. 5 (18) (2009) 3377–3384, https://doi.org/10.1039/b904493k.
[8] W.C. Nelson, C.J.C. Kim, Droplet actuation by electrowetting-on-dielectric (EWOD): a review, J. Adhes. Sci. Technol. vol. 26 (12–17) (2012) 1747–1771, https://doi.org/10.1163/156856111×599562.
[9] F. Mugele, J.C. Baret, Electrowetting: from basics to applications, J. Phys. Condens. Matter vol. 17 (28) (2005), https://doi.org/10.1088/0953-8984/17/28/R01.
[10] H.M. Silalahi, Y.-H. Tsai, K.-L. Lee, P.-K. Wei, C.-Y. Huang, Large shift of resonance wavelengths of silver nanoslit arrays using electrowetting-on-dielectric cells, Opt. Lett. vol. 46 (4) (2021) 705–708, https://doi.org/10.1364/OL.415500.
[11] H.M. Silalahi, Y.-H. Shih, S.-H. Lin, Y.-T. Chen, W.-Y. Wei, P.-L. Chao, C.-Y. Huang, Electrically controllable terahertz metamaterials with large tunabilities and low operating electric fields using electrowetting-on-dielectric cells, Opt. Lett. vol. 46 (23) (2021) 5962–5965, https://doi.org/10.1364/OL.444842.
[12] P.Y. Chiou, H. Moon, H. Toshiyoshi, C.J. Kim, M.C. Wu, Light actuation of liquid by optoelectrowetting, Sens. Actuators A Phys. vol. 104 (3) (2003) 222–228, https://doi.org/10.1016/S0924-4247(03)00024-4.
[13] S.N. Pei, J.K. Valley, Y.L. Wang, M.C. Wu, Distributed circuit model for multi-color light-actuated opto-electrowetting microfluidic device, J. Light. Technol. vol. 33 (16) (2015) 3486–3493, https://doi.org/10.1109/JLT.2015.2405076.
[14] J. Loo, S.N. Pei, M.C. Wu, Co-planar light-actuated optoelectrowetting microfluidic device for droplet manipulation, J. Opt. Microsyst. vol. 1 (03) (2021) 1–16, https://doi.org/10.1117/1.jom.1.3.034001.
[15] J. Loo, Co-planar Optoelectrowetting (OEW) Device for Droplet Manipulation, 2020, [Online]. Available: http://www2.eecs.berkeley.edu/Pubs/TechRpts/2020/EECS-2020-213.html.
[16] J. Strassner, C. Doering, E. Oliveira, H. Fouckhardt, Optoelectrowetting (OEW) with push-actuation of microdroplets at small frequencies and OEW equations revisited, Sens. Actuators A Phys. vol. 334 (2022), 113331, https://doi.org/10.1016/j.sna.2021.113331.
[17] A. Quinn, R. Sedev, J. Ralston, Contact angle saturation in electrowetting, J. Phys. Chem. B vol. 109 (13) (2005) 6268–6275, https://doi.org/10.1021/jp040478f.
[18] R. Zhao, Z.C. Liang, Mechanism of contact angle saturation and an energy-based model for electrowetting, Chin. Phys. B vol. 25 (6) (2016), https://doi.org/10.1088/1674-1056/25/6/066801.
[19] D. Klarman, D. Andelman, A model of electrowetting, reversed electrowetting, and contact angle saturation, Langmuir vol. 27 (10) (2011) 6031–6041, 10.1021/la2004326.
[20] A.I. Drygiannakis, A.G. Papathanasiou, A.G. Boudouvis, On the connection between dielectric breakdown strength, trapping of charge, and contact angle saturation in electrowetting, Langmuir vol. 25 (1) (2009) 147–152, https://doi.org/10.1021/la802551j.
[21] I.E. Markodimitrakis, D.G. Sema, N.T. Chamakos, P. Papadopoulos, A. G. Papathanasiou, Impact of substrate elasticity on contact angle saturation in electrowetting, Soft Matter vol. 17 (16) (2021) 4335–4341, https://doi.org/10.1039/d0sm02281k.
[22] G. Hughes, C. Springer, U. Resch, N. Esser, W. Richter, A reflectance anisotropy spectroscopy study of molecular sulfur adsorption on the GaAs(100) surface, J. Appl. Phys. vol. 78 (3) (1995) 1948–1952, https://doi.org/10.1063/1.360234.

[23] S. Chevalliot, S. Kuiper, J. Heikenfeld, Experimental validation of the invariance of electrowetting contact angle saturation, J. Adhes. Sci. Technol. vol. 26 (12–17) (2012) 1909–1930, https://doi.org/10.1163/156856111×599580.
[24] P. Teng, D. Tian, H. Fu, S. Wang, Recent progress of electrowetting for droplet manipulation: from wetting to superwetting systems, Mater. Chem. Front. vol. 4 (1) (2020) 140–154, https://doi.org/10.1039/c9qm00458k.
[25] F. Krogmann, H. Qu, W. Mönch, H. Zappe, Push/pull actuation using opto-electrowetting, Sens. Actuators A Phys. vol. 141 (2) (2008) 499–505, 10.1016/ j.sna.2007.08.017.
[26] Y.Y. Lin, R.D. Evans, E. Welch, B.N. Hsu, A.C. Madison, R.B. Fair, Low voltage electrowetting-on-dielectric platform using multi-layer insulators, Sens. Actuators B Chem. vol. 150 (1) (2010) 465–470, https://doi.org/10.1016/j.snb.2010.06.059.
[27] J.H. Song, R. Evans, Y.Y. Lin, B.N. Hsu, R.B. Fair, A scaling model for electrowetting-on-dielectric microfluidic actuators, Microfluid. Nanofluidics vol. 7 (1) (2009) 75–89, https://doi.org/10.1007/s10404-008-0360-y.
[28] H. Ren, R.B. Fair, M.G. Pollack, E.J. Shaughnessy, Dynamics of electro-wetting droplet transport, Sens. Actuators B Chem. vol. 87 (1) (2002) 201–206, https://doi.org/10.1016/S0925-4005(02)00223-X.
[29] C. Doering, J. Strassner, H. Fouckhardt, Lithography-free technology for the preparation of digital microfluidic (DMF) lab-chips with droplet actuation by optoelectrowetting (OEW), Int. J. Anal. Chem. vol. 2022 (2022), https://doi.org/10.1155/2022/2011170.
[30] S. Singer, J. Nelder, Nelder-Mead algorithm, Scholarpedia vol. 4 (7) (2009), 2928, https://doi.org/10.4249/scholarpedia.2928.
[31] F. Gao, L. Han, Implementing the Nelder-Mead simplex algorithm with adaptive parameters, Comput. Optim. Appl. vol. 51 (1) (2012) 259–277, doi: 10.1007/s10589-010-9329-3.
[32] M.H. Wright, Direct Search Methods Once Scorned Now Respectable, Technical Report 96-4-02, Computing Science Research Center, AT&T Bell Laboratories, Murray Hill, NJ, 1996.
[33] P. Virtanen, et al., SciPy 1.0: fundamental algorithms for scientific computing in python, Nat. Methods vol. 17 (3) (2020) 261–272, https://doi.org/10.1038/s41592-019-0686-2.

E. Oliveira (born 1994 in Santo André, Brazil) earned a Bachelor's degree in Materials Engineering from Universidade Presbiteriana Mackenzie in 2017 and a Master's degree in Electrical Engineering from the same university in 2020. He completed his Ph.D. in Physics at the University of Kaiserslautern in 2023. Following his Ph.D., he conducted a short postdoctoral research in the same working group at the University of Kaiserslautern. Emerson is currently employed by Laytec in Berlin.

C. Doering (born 1978 in Rockenhausen, Germany) received his Ph.D. degree in physics with a focus on high power semiconductor lasers from Technische Universität Kaiserslautern (TUK), Germany in 2007. He works as a senior scientist in the research group of Henning Fouckhardt and lab manager in the physics department. His research interests include applied physics, optoelectronic materials, semiconductor lasers, and technology.

H. Fouckhardt (born 1959 in Hannover, Germany) has studied physics at the University of Goettingen in Germany, finishing with a Ph.D. degree in 1987. Then for one year he became a postdoc with Bell Communications Research (Bellcore) Inc. in Red Bank, New Jersey, USA. From 1989–1991, he was a member of scientific staff in Hewlett Packard's Analytical Divison in Waldbronn, Germany. In 1991, H. Fouckhardt became an Associate Professor in the Electrical Engineering Department of the Technical University Braunschweig, Germany, heading the research group Integrated Optoelectronics. In 1996, he became a full professor and got a chair in Technical and Experimental Physics at the Technische Universität Kaiserslautern (TUK), Germany.